



Formation of Laser-Induced Periodic Surface Structures on Reaction-Bonded Silicon Carbide by Femtosecond Pulsed Laser Irradiation

Tushar Meshram¹ · Jiwang Yan²

Received: 8 October 2022 / Revised: 20 November 2022 / Accepted: 4 January 2023
© The Author(s) 2023

Abstract

Reaction-bonded silicon carbide (RB-SiC) is an excellent engineering material with high hardness, stiffness, and resistance to chemical wear. However, its widespread use is hindered due to the properties mentioned above, making it difficult to machine functional surface structures through mechanical and chemical methods. This study investigated the fundamental characteristics of laser-induced periodic surface structures (LIPSSs) on RB-SiC via femtosecond pulsed laser irradiation at a wavelength of 1028 nm. Low-spatial-frequency LIPSS (LSFL) and high-spatial-frequency LIPSS (HSFL) formed on the surface along directions perpendicular to the laser polarization. SiC grains surrounded by a large amount of Si show a reduced threshold for LIPSS formation. By varying laser fluence and scanning speed, HSFL–LSFL hybrid structures were generated on the SiC grains. Transmission electron microscopy observations and Raman spectroscopy were carried out to understand the formation mechanism of the hybrid LIPSS. A possible mechanism based on the generation of multiple surface electromagnetic waves due to the nonlinear response of SiC was proposed to explain the hybrid structure formation. Furthermore, the direction of laser scanning with respect to laser polarization affects the uniformity of the generated LIPSS.

Highlights

- 1 LIPSS formation on a composite material with significantly different optical properties of constituent materials.
- 2 Hybrid nanostructure formation due to the generation of surface electromagnetic waves.
- 3 Effect of nonlinear change in material property on LIPSS formation due to harmonic generation.

Keywords Reaction-bonded silicon carbide · Surface texturing · Laser-induced periodic surface structure · Composite material · Hybrid nanostructure

1 Introduction

Reaction-bonded silicon carbide (RB-SiC) is an excellent engineering material with high hardness and is resistant to chemical wear. Thus, it is widely employed in various applications requiring wear and corrosion resistance. Due to its high thermal conductivity and low thermal expansion coefficient, RB-SiC components are widely used in thermal management or heat dissipation applications, such as high voltage power supply and heat exchanger tubing. RB-SiC is also used to make molds for manufacturing glass lenses via

✉ Jiwang Yan
yan@mech.keio.ac.jp

¹ School of Integrated Design Engineering, Graduate School of Science and Technology, Keio University, Hiyoshi 3-14-1, Kohoku-ku, Yokohama 223-8522, Japan

² Department of Mechanical Engineering, Faculty of Science and Technology, Keio University, Hiyoshi 3-14-1, Kohoku-ku, Yokohama 223-8522, Japan

press molding, optical mirrors, and structural components [1, 2].

However, processing RB-SiC is very difficult as the unique properties that make it a desirable material also make it very difficult to machine through mechanical and chemical methods. Furthermore, RB-SiC is a composite consisting of two different phases in which SiC grains are held together by a Si matrix. Si and SiC have very different mechanical and chemical properties, which adds to the complexity of processing RB-SiC and makes it difficult to generate uniform surface structures [3–5]. There is a growing demand for micro- and nanostructured surfaces in most of the above-mentioned applications, as the generation of these structures can drastically improve and enhance desirable properties, such as reflectivity, heat dissipation, coefficient of friction, and surface wettability [6–10].

Laser processing can be a very effective method of creating such surface structures as laser interaction with the material is a non-contact process and hence is not affected by the material's hardness and chemical inertness. In the past decade, laser-induced periodic surface structures (LIPSSs) have been extensively studied to create functional surfaces. LIPSSs can be divided into two categories based on their periods (Λ) [11]. First, when the period is near the wavelength of the laser ($\Lambda_{\text{LSFL}} \sim \lambda$), they are called low-spatial-frequency LIPSSs (LSFLs) and are mostly known to form highly absorptive materials, such as metal and semiconductors (laser photon energy \approx bandgap) [12]. The most widely accepted mechanism for LSFL formation is the interaction of laser with surface electromagnetic waves (SEWs) [13], which results in the selective ablation of the surface, resulting in LSFL formation. Second, when the period is much smaller than the wavelength of the laser ($\Lambda_{\text{HSFL}} \ll \lambda$), they are called high-spatial-frequency LIPSSs (HSFLs) and are known to form weak absorptive and transparent materials, such as dielectric and semiconductors (laser photon energy \ll bandgap) [12]. Although the exact mechanism is still under debate, HSFLs are usually attributed to the generation of surface plasmon polaritons (SPPs), self-organization, and second-harmonic generation [14, 15]. LIPSS formation on metals has been extensively investigated [16–19]. While SPP can ideally only propagate between metal and dielectric interface [20], SPPs can be generated on semiconductors via laser irradiation. Laser irradiation on semiconductors with ultrashort pulses results in the generation of free electrons near the surface, thus attaining a metal-like state [11, 21–23]. However, the number of electrons that will be generated is affected by the bandgap of the semiconductor and the wavelength of the laser.

There have been many research works on LIPSS formation on silicon and a few on silicon carbide [21, 24, 25], but

there are no studies reported on LIPSS formation on RB-SiC, as per the author's best knowledge. Si and SiC have different optical properties and bandgaps, so they interact differently with the same laser. Hence, understanding laser interaction with this two-phase material is crucial for creating functional surfaces to meet the current demand for textured surfaces and boosting the widespread use of RB-SiC in industries.

Hence, in this study, we investigated the fundamental characteristics of LIPSS formation on RB-SiC via femto-second pulsed laser irradiation. The effect of laser irradiation on Si and SiC under the same laser parameters is discussed based on transient material properties due to spatial and temporal changes in the laser intensity and wavelength/energy of laser photons. The objective is to clarify the mechanism of various LIPSS formations that occur on RB-SiC based on material properties and laser parameters.

2 Materials and Method

2.1 Materials

The RB-SiC sample used in this research was cylindrical with a diameter of 5 cm and a height of 15 mm. The sample surface was polished, and the surface roughness was 14 nm Ra. Figure 1a shows an electron microscope image of the RB-SiC sample captured using a circular backscattering detector. The black region is SiC carbide grains, and the white region is a Si matrix. The Si matrix showed a typical Raman shift for single-crystal silicon, whereas the SiC grains showed a typical Raman shift for 6H-SiC, as shown in Fig. 1b.

2.2 Laser Irradiation Setup and Conditions

The laser used in the experiments was PHAROS-08-600-PP manufactured by Light Conversion, Lithuania. The laser had a wavelength of 1028 nm and can create ultrashort pulses with a width of 256 fs at a pulse frequency of 100 kHz. The laser scanning was controlled using a galvanometer scanning system, and the laser was focused on the sample using an f-theta lens. The focused spot was elliptical with a Gaussian distribution and had major and minor axis diameters of 23 and 17.4 μm , respectively. The major axis was parallel to the polarization direction.

All the experiments in this study were performed in atmospheric conditions at room temperature ($\sim 23^\circ\text{C}$). Two types of experiments were carried out in this research. The first type was line irradiation, in which a laser spot was

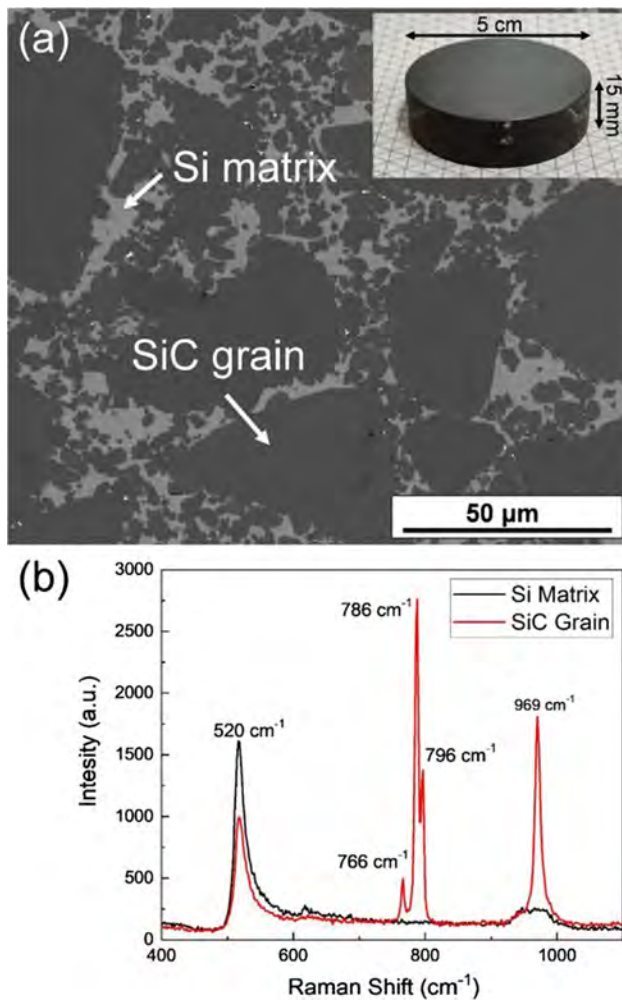


Fig. 1 **a** Photo of the RB-SiC sample and SEM image of the original surface, **b** Raman spectra of the Si matrix and SiC grain

scanned in a line at various scanning speeds, fluences, and numbers of scans. The second type was spot irradiation, in which the laser was irradiated for a set amount of time to control the number of pulses irradiated on the sample. Important laser parameters for the above experiments are shown in Table 1.

Table 1 Experimental conditions

Laser medium	Yb: KGW
Wavelength [nm]	1028
Spot size [μm]	23×17.4
Pulse width [fs]	256
Repetition frequency [kHz]	100
Scanning speed [mm/s]	10–100
Laser fluence [J/cm^2]	0.16–1.59
Number of irradiations (N_{irrad})	1, 5

2.3 Measurement and Characterization Methods

After the laser irradiation experiment, the sample was wiped with ethanol using a cotton bud and then cleaned using an ultrasonic cleaner to remove any deposited debris. After cleaning, surface structures were observed using a field emission scanning electron microscope (FE-SEM) Inspect F50, manufactured by FEI Company, USA. The material composition was measured using the Raman spectroscopy instrument (inVia™ confocal Raman microscope made by Renishaw plc, England), with a laser wavelength of 512 nm and measurement spot diameter of 1 μm . To observe the cross-section of the LIPSS structure, after the LIPSS formation, the surface was cleaned and coated with a protective Pt coating, and then a focused ion beam was used to cut and create a thin sample. Then, the sample was observed using a transmission electron microscope (TEM), Tecnai G2, made by FEI Company, USA. In addition, elemental distribution was studied using an energy-dispersive X-ray spectroscopy (EDX) module attached to the TEM equipment.

3 Results and Discussion

3.1 Effect of Laser Fluence

Line irradiation was performed to observe the effect of laser fluence on the LIPSS formation. The laser scanning speed was 60 mm/s, and $N_{\text{irrad}} = 1$. The scanning direction was perpendicular to the polarization direction. The SEM images of the LIPSS formed at various fluences are shown in Fig. 2. When the fluence was 0.16 J/cm^2 (Fig. 2a), the

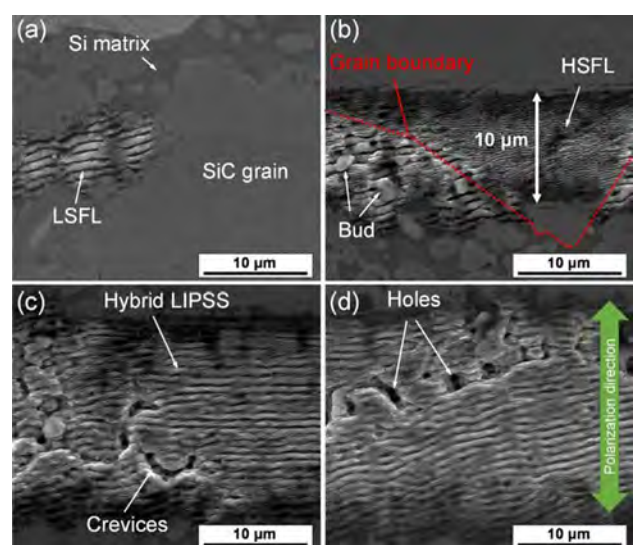


Fig. 2 SEM images of line irradiation at a scanning speed of 60 mm/s and fluences of **a** 0.16, **b** 0.32, **c** 0.95, and **d** 1.59 J/cm^2

LIPSS did not form on SiC grains and LSFLs with a period of 850 ± 25 nm were observed on the Si matrix. The width of the peaks is approximately 600 nm, whereas that of the valleys is approximately 250 nm. As the fluence was increased to 0.32 J/cm^2 (Fig. 2b), the LSFL structures on Si partially melted into liquid Si. This molten Si agglomerated to form bud shapes due to surface tension. Meanwhile, HSFLs with a period of 225 ± 25 nm were observed on the SiC grains. The width of the peaks is approximately 125 nm, whereas that of the valleys is approximately 100 nm. LSFLs and HSFLs formed perpendicular to the direction of laser polarization. The reason for the LIPSS formation with a different period on Si and SiC is that the energy of laser photons (1.2 eV) used in this research is close to the bandgap of Si (1.1 eV). Thus, Si showed a high absorptivity coefficient for this wavelength. However, SiC is a high bandgap (3.023 eV) semiconductor and has a very low coefficient of absorption for the laser wavelength used in this study. The difference in the absorptivity coupled with the difference in the relative permittivity (Si: $\epsilon_\infty = 12.8$, SiC: $\epsilon_\infty = 6.98$) [26, 27] resulted in the formation of SPPs with a different period on SiC as compared to that on Si (Fig. 3). As laser interacts with generated SPPs, it creates a different interference pattern on SiC than that on Si, resulting in the formation of LSFLs on Si and HSFLs on SiC. On SiC grains, HSFLs only formed in the central region of the laser-irradiated area with a width of approximately $10 \mu\text{m}$. However, when SiC was surrounded by a large amount of Si, HSFL formation was observed in a broader region beyond the width of a $10 \mu\text{m}$ range. The thermal effect and electron movement from Si might have reduced the threshold for the HSFL formation on SiC.

As the fluence was further increased (Fig. 2c, d), the Si regions were significantly ablated, resulting in the formation of crevices and holes. This selective ablation is thought to be because of the difference in the evaporation temperature. In the case of SiC grains, HSFL structures agglomerated to form LSFLs in the center of the irradiated region, whereas only HSFL structures occurred near the boundary of the irradiated region. This condition is thought to be due to the Gaussian nature of the fluence distribution. In Fig. 2c, a hybrid of HSFLs and LSFLs can be observed. In Fig. 2d, only LSFLs are observed. A similar LSFL formation at a high fluence has been previously reported on SiC [28].

Other researchers have reported the formation of independent LSFLs and HSFLs on various materials, such as

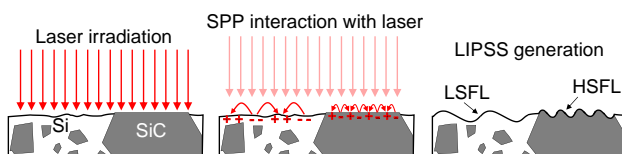


Fig. 3 Mechanism of LIPSS formation on RB-SiC

SiC, ZnO, InP, fused silica, and Ge [14, 15, 29–33], but the hybrid structures of LSFLs and HSFLs shown in Fig. 2 have not been reported before. There are two possible reasons for the transformation of HSFLs into LSFLs. The first is the thermal decomposition of SiC into Si and C. Thus, Si and SiC are present locally in a very small area, which results in the formation of hybrid LIPSSs. As the fluence is further increased, SiC is completely decomposed to Si. Thus, at a high fluence, only an LSFL is observed at the center of the irradiated area. The second is the generation of two different SPP waves in SiC without thermal decomposition. The absorption coefficient of SiC for a given wavelength of the photon is temperature dependent. Hence, with a pulse overlap, the temperature of SiC increases, resulting in an increased number of generated free electrons. The increase in electron density led to the formation of a different SPP waves, and consequently the formation of a hybrid LIPSS.

3.2 Effect of Laser Scanning Speed

Line irradiation was performed for various scanning speeds at a fluence of 0.95 J/cm^2 and $N_{\text{irad}} = 1$. Figure 4 shows the SEM images of the LIPSS formation. At a laser scanning speed of 10 mm/s (Fig. 4(a)), there was almost no sign of LIPSS formation. Instead, a groove was formed on the surface. The groove wall was covered with fine granular structures, which are thought to be reattached debris after laser irradiation. At 40 mm/s (Fig. 4b), hybrid LIPSS structures can be observed with holes formed in Si matrix regions. In Fig. 4c and d, the HSFL–LSFL hybrid structures did not form in the central region. Instead, an LSFL was generated.

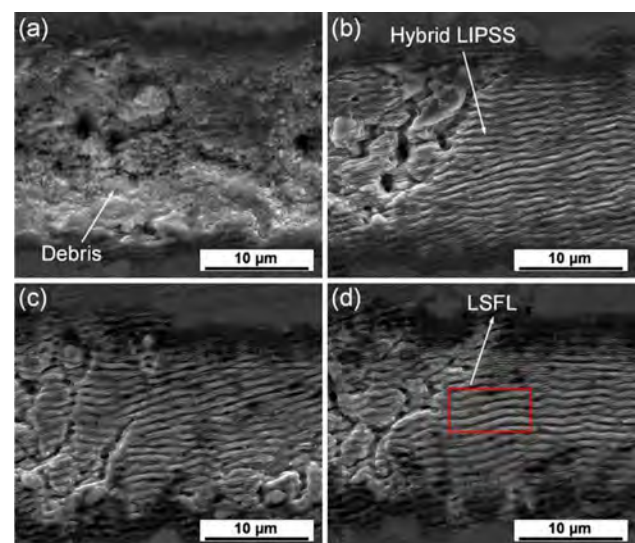


Fig. 4 SEM images of line irradiation with a fluence of 0.95 J/cm^2 and scanning speeds of **a** 10, **b** 40, **c** 80, and **d** 100 mm/s

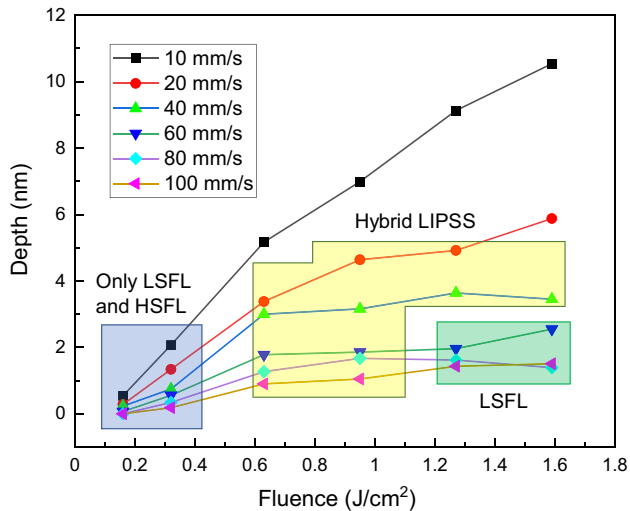


Fig. 5 Type of LIPSS formation at various laser fluences and scanning speeds

Figure 5 shows the ranges of laser fluences and scanning speeds at which different types of LIPSSs formed. For all scanning speed conditions at low fluences (highlighted in the blue-color area in Fig. 5), LSFLs and HSFLs formed separately, as shown in Fig. 2b. As the fluence was increased, LIPSSs did not form at lower speeds (highlighted in yellow in Fig. 5), whereas the hybrid LIPSS formed, as shown in Fig. 4b and c. Although the hybrid LIPSSs look similar, the depth at which they form for a given laser fluence is

dependent on the scanning speed. At a high fluence and high scanning speed (highlighted in the green-color area in Fig. 5), the hybrid LIPSS did not form; instead, only an LSFL was observed.

3.3 Effect of Laser Scanning Direction

Line irradiation was carried out at a laser fluence of 0.63 J/cm^2 , and the laser beam was scanned one time at a speed of 100 mm/s . The scanning direction (indicated by the white arrow in Figs. 6 and 7) was changed from parallel to the laser polarization direction to perpendicular to the polarization direction. The hybrid LIPSSs formed in Fig. 6a are clear, ordered, and continuous. As the angle between the laser polarization and laser scanning direction was increased, a zip-like structure was observed, the frequency of which also increased (from Fig. 6b–e). Due to the Gaussian nature of the laser fluence inside the spot, the peak SPP intensity was generated near the central region. When the laser was scanned at an angle, the peak intensity region was slightly shifted at an angle, which created a mismatch between the SPP propagation directions, resulting in the formation of a zip-like structure. Finally, when the laser scanning direction was perpendicular to the laser polarization, the hybrid LIPSSs formed were nonuniform and predominantly formed in the central region, whereas the edge regions had an HSFL (Fig. 6f). This result suggests that the intensity of SPPs generated when the laser was scanned parallel to the polarization direction was much stronger.

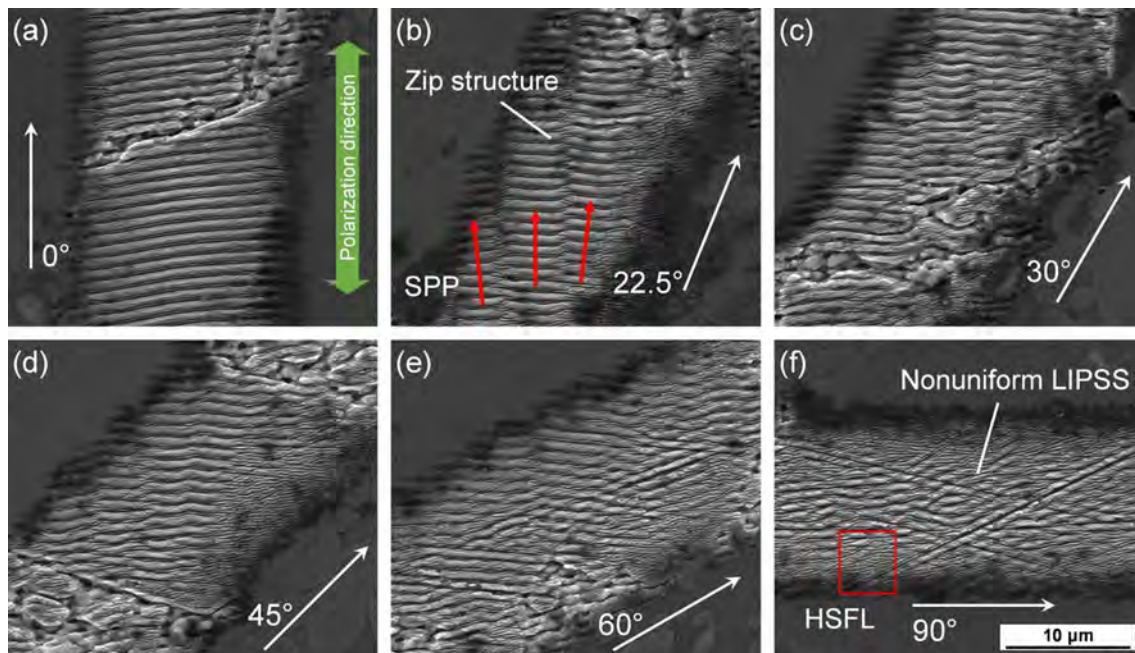


Fig. 6 SEM images of line irradiation with laser scanning directions of **a** 0° , **b** 22.5° , **c** 30° , **d** 45° , **e** 60° , and **f** 90° to the laser polarization direction

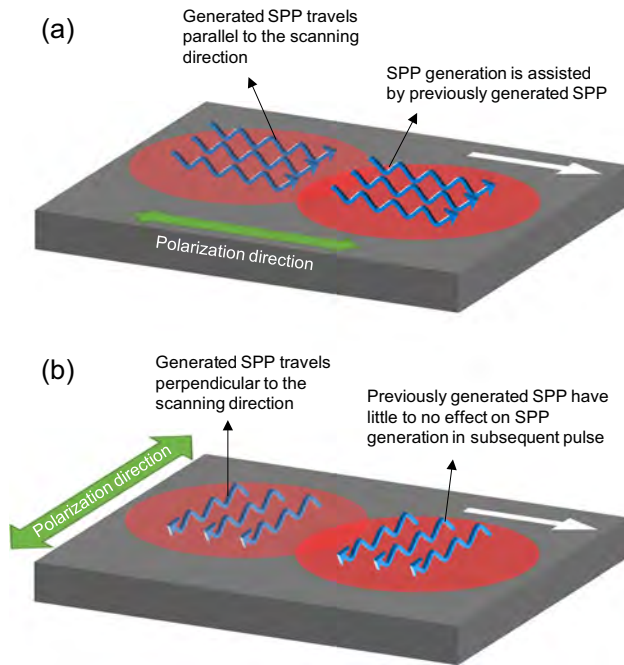


Fig. 7 Schematic diagram of the SPP formation and propagation when polarization and scanning direction is **a** parallel and **b** perpendicular.

The difference in the generated intensity is due to the formation and decay of SPPs. As presented in Fig. 7, when the laser is scanned perpendicular to the polarization direction, the generated SPP is parallel to the polarization direction (for Si and SiC). As the laser moved ahead, the SPP was generated in a new location, and the previously generated SPP decayed, which led to the non-uniformity of the SPP intensity in the laser scanning direction, resulting in a zip structure formation. Meanwhile, when the laser was scanned parallel to the polarization direction, the generated SPP was in the same direction as the laser movement, and hence the excitation and propagation of subsequent SPPs were assisted by previously generated SPPs [34, 35]. This condition leads to the formation of clear, continuous, and uniform LIPSSs.

3.4 Effect of Repetitive Scans

Figure 8 shows the SEM images of surfaces line-irradiated with a scanning speed of 100 mm/s and $N_{\text{irad}} = 1, 5$. At a low fluence of 0.32 J/cm^2 (Fig. 8a, b), the increase in the scanning repetition caused Si to melt and agglomerate. This outcome is because the laser fluence can melt silicon but is not enough to vaporize it, thus leading to the agglomeration of molten silicon. A slight ablation occurred on the SiC grains, but HSFL structures remained on the surface. At a high fluence of 1.62 J/cm^2 (Fig. 8c, d), an increase in the scanning

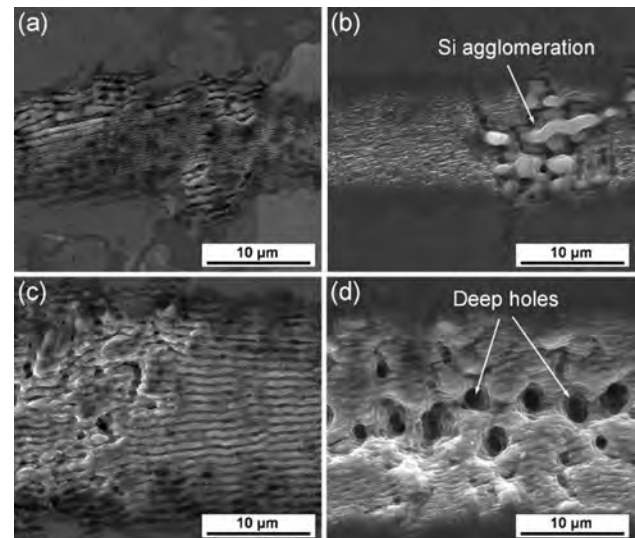


Fig. 8 SEM images of line irradiation when laser was scanned **a, c** 1 and **b, d** 5 times

repetition led to the complete removal of Si from the surface, which resulted in the formation of deep holes. Moreover, due to the ablation of SiC grains, the LSFL structures became less defined and shallower.

4 Material Structure Analysis of LIPSSs

4.1 Raman Spectroscopy

Figure 9 shows the typical Raman spectra of LSFL, HSFL, and HSFL–LSFL hybrid structures. Line irradiation was carried out with a scanning speed of 10 mm/s and fluence of 0.16 J/cm^2 . The Raman shift obtained for the LSFL structures was 515 cm^{-1} , which was near the Raman shift of the single-crystal Si (521 cm^{-1}), whereas the HSFL structures showed a Raman shift of 6H–SiC ($768, 789, \text{ and } 967 \text{ cm}^{-1}$). Thus, the result confirms that LSFL structures are formed in the Si matrix regions and HSFL structures on the SiC grains. However, the Raman shift for the HSFL–LSFL hybrid structures (Fig. 6a) also showed a Raman shift of 6H–SiC, although a small peak of Si can be observed around 520 cm^{-1} . The Raman measurement area had a diameter of $1 \mu\text{m}$. Hence, a much stronger intensity of the Raman peak for Si would be observed as the LSFL structure covers most of the surface in the hybrid LIPSS structure, as marked in Fig. 9b. However, from a very small intensity of the Raman shift for Si, it is hypothesized that hybrid LIPSS structures consist of single-crystal SiC.

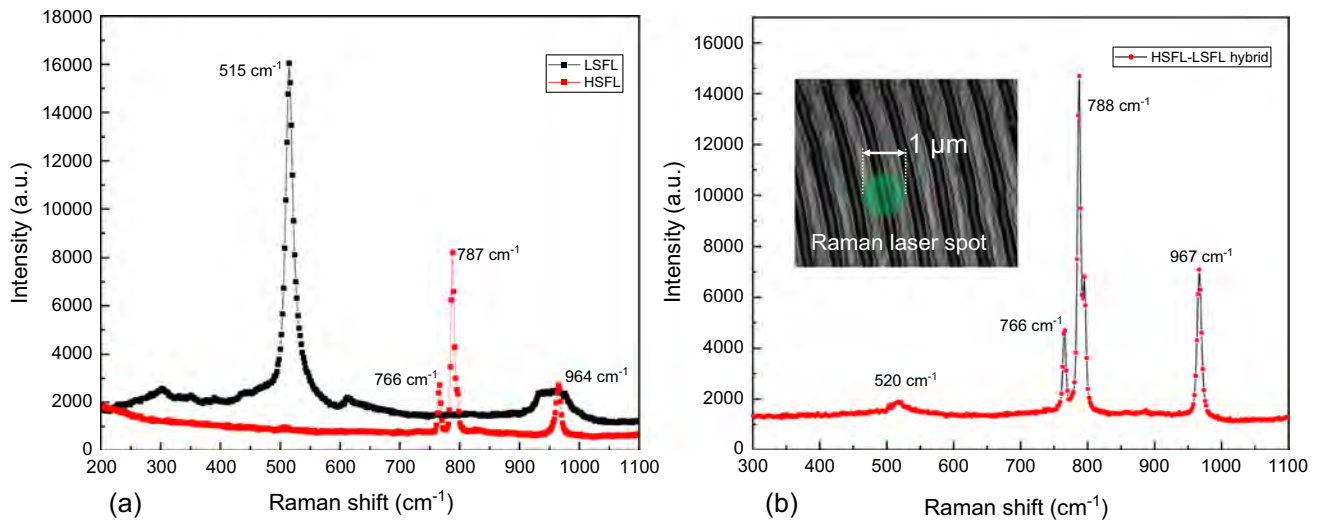


Fig. 9 Raman spectroscopy analysis of **a** regular and **b** hybrid LIPSS

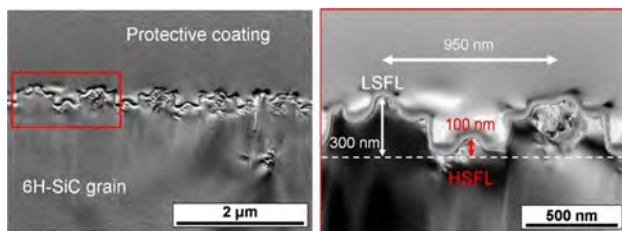


Fig. 10 TEM cross-section image of the hybrid LIPSS generated at a fluence of 0.63 J/cm^2 and scanning speed of 100 mm/s , scanned perpendicular to the laser polarization direction

4.2 TEM Observation and EDX Analysis

A hybrid LIPSS generated at a fluence of 0.63 J/cm^2 and scanning speed of 100 mm/s , scanned perpendicular to the laser polarization direction (Fig. 6a), was chosen for the TEM analysis. The cross-sectional images of the hybrid LIPSS are shown in Fig. 10. The hybrid LIPSS consists of two different size levels. A small bud-shaped HSFL formed between two LSFLs with a height of 100 nm . The LSFL had a head and shoulder structure, and the center peak (head) was approximately 300 nm from the base. Meanwhile, the shoulders were around 200 nm high. The LSFL and HSFL in the hybrid LIPSS formed within a period of $\sim 950 \text{ nm}$, similar to the LSFL formed in the Si region at low fluence. The distance between the head and shoulder and the shoulder and HSFL was approximately $\sim 220 \text{ nm}$, similar to the HSFL formed on SiC grains at low fluence. This similarity in periodicity could be a result of the hybrid LIPSS formation due to the interference between laser and HSFL and LSFL forming SPP waves.

A high magnification was used to observe the lattice structure and composition. As marked in Fig. 11, four locations are observed: head, shoulder on the LSFL, HSFL, and bulk material. The fast Fourier transformation method was used to determine the lattice spacing, and it was found that all four locations have a crystalline structure. Furthermore, the crystal orientation was the same for all four locations, with a lattice spacing of 2.33 \AA . The depth of the bulk material was sufficiently deep, which would not be affected by the laser parameters used in this experiment. Thus, the hybrid LIPSS is a part of a single 6H-SiC grain rather than a result of the thermal decomposition of SiC into Si and C. However, for such a hybrid structure to form, it can be safely assumed that two different SPP waves were generated on SiC, which resulted in the formation of a hybrid LIPSS.

Figure 12 shows the EDX spectroscopy result of the hybrid LIPSS. The hybrid LIPSS does not have any localized patches of only Si or C, and the region has Si and C, which is consistent with the TEM observation that a hybrid LIPSS is made up of SiC.

5 LIPSS Formation Mechanism

5.1 Spatial and Temporal Changes in Laser Intensity

As shown in Sect. 3.1, the HSFL formed at a low laser fluence, and the LSFL formed at a high laser pulse fluence on the SiC grains. It is hypothesized that this difference in results is due to the nonlinear optical response of SiC. The refractive index and absorption coefficient can change nonlinearly due to various factors, such as the intensity of the

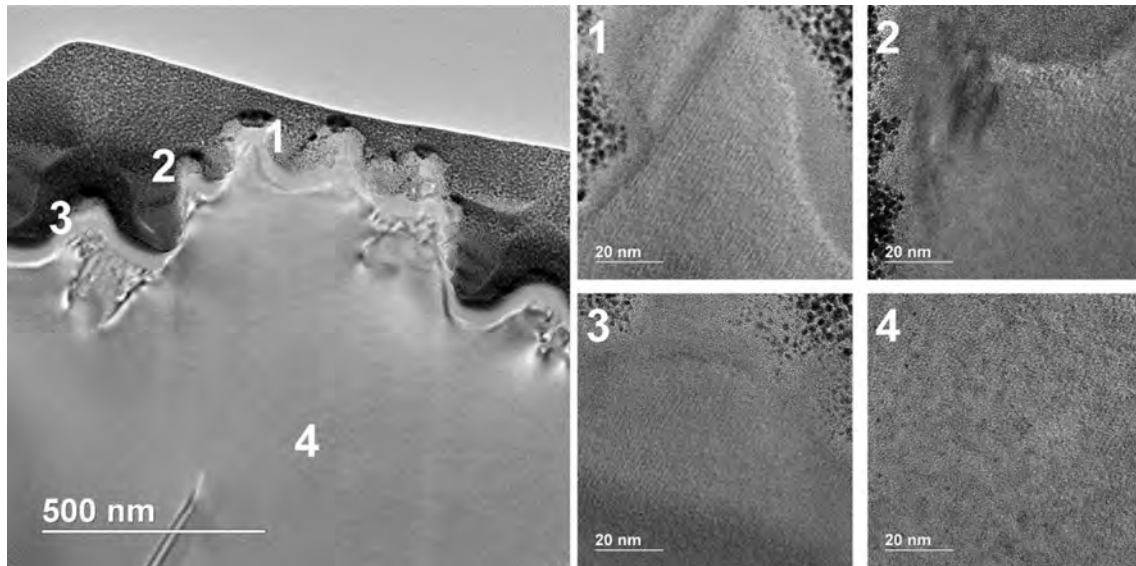


Fig. 11 TEM cross-section image of hybrid LIPSS with locations marked **1** head, **2** shoulder, **3** HSFL and **4** bulk material

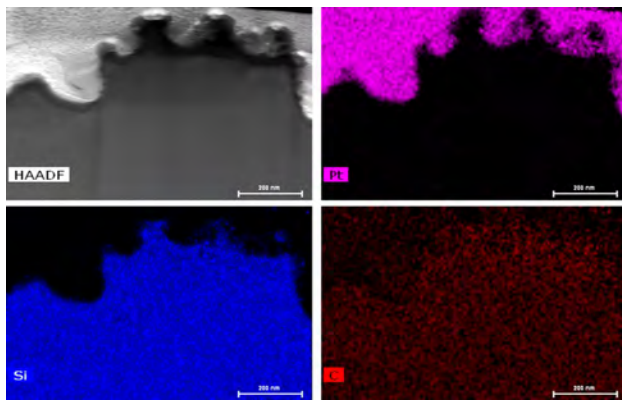


Fig. 12 Energy-dispersive X-ray spectroscopy image of hybrid LIPSS cross-section

external electric field and free carrier generation [31]. The period of the LIPSS generated on semiconductors is related to the refractive index of the material [12, 24, 31, 36].

The laser pulse fluence is the average energy per unit area. However, to understand the mechanism of LIPSS formation based on nonlinear changes in the material properties, laser intensity (energy per unit area per unit time) is a better parameter. The laser spot had a Gaussian power distribution; hence the laser intensity at the center of the laser spot is much higher as compared to the edges. In addition, the laser intensity varies temporally during the laser pulse. The spatial and temporal changes in intensity produce a transient change in optical properties, which in turn affects the LIPSS generation. SiC shows a high third-order nonlinear susceptibility ($\chi^{(3)}$), which means that the

optical properties of SiC change with the intensity of the light source. F. De Leonadis et al. showed that SiC exhibits the Kerr effect, which is a result of the third-order nonlinear susceptibility [37, 38]. This nonlinear susceptibility results in the third-harmonic SPP generation, i.e., a surface wave with a wavelength of $\frac{\lambda}{3}$ is generated from a wave with a wavelength of λ [39, 40]. D. Dufft et al. reported the existence of second-harmonic generation by spectroscopically measuring radiation emitted from a laser irradiation spot where the HSFL was generated on ZnO [15]. In our case, the period of the HSFL is around one-third of the period of the generated LSFL, i.e., $\Lambda_{HSFL} \approx \frac{\Lambda_{LSFL}}{3}$. Thus, the HSFL formation on SiC in the low laser intensity region is due to the third-harmonic surface plasmon generation. However, this harmonic generation is limited to near or below the ablation threshold. As the number of free charge carriers increases, SiC starts to behave like a metal, which is known for LSFL generation due to the near-laser-wavelength SPP formation.

$$I_{(r)} = I_{t,Max} e^{-2\left(\frac{r}{b}\right)^2} \tag{1}$$

$$I_{(t)} = \frac{2P_0 e^{-0.5\left(\frac{t-\tau}{\tau}\right)^2}}{\pi b^2} \tag{2}$$

Equation 1 maps the laser intensity along the radial direction, where $I_{t,Max}$ is the peak intensity at a given time, b is the radius of the laser, and r is the variable radial distance. Equation 2 is the temporal change in the laser intensity, where P_0 is the peak power, τ is the laser pulse width, and t

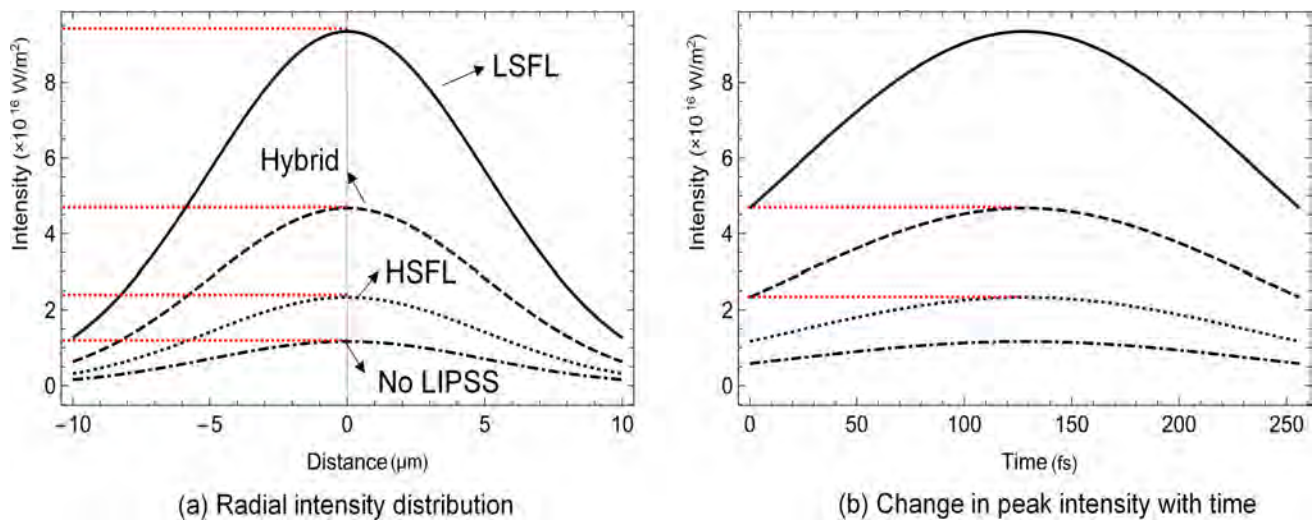


Fig. 13 Laser intensity distribution: **a** spatial and **b** temporal changes in the peak intensity

is the time. Figure 13a shows the intensity distribution along the radial direction, and Fig. 13b shows the change in the peak intensity with time at the center of the spot.

The peak intensity at which only the HSFL was observed is $I_{\text{HSFL}} = 2.34 \times 10^{16} \text{ W/m}^2$. This is comparable to the intensity around the edges of the laser spot when the peak intensity was high enough to form an LSFL, i.e., $I_{\text{LSFL}} = 9.35 \times 10^{16} \text{ W/m}^2$. This explains the reason for the HSFL formation even at a very high fluence. Interestingly, the HSFL only formed in the region that had a fluence above the peak intensity of $I_{\text{no_LIPSS}} = 1.17 \times 10^{16} \text{ W/m}^2$, as shown in Fig. 3b. The peak intensity at which hybrid LIPSSs were generated is $I_{\text{Hybrid}} = 4.67 \times 10^{16} \text{ W/m}^2$, which is around half the intensity of I_{LSFL} . During the I_{Hybrid} peak intensity, around half of the laser spot has an intensity around I_{HSFL} . The I_{Hybrid} intensity is high enough to cause a two-photon or three-photon excitation [31]. The change in the peak intensity along the time/pulse width shows that the lowest intensity of I_{LSFL} is almost the same as the peak intensity value, as shown in Fig. 13b. Similarly, the peak intensity of I_{HSFL} is comparable to the lowest intensity of I_{Hybrid} , which suggests that in the case of I_{Hybrid} , the central location of the laser spot can first observe HSFL formation, then LSFL formation, and finally HSFL formation.

5.2 Spot Irradiation Phenomena

A spot irradiation experiment was designed to confirm the hypothesis that a nonlinear response due to the laser intensity is the reason that different LIPSSs form at low and high pulse fluences and further improve understanding of the mechanism of hybrid LIPSS formation. Figure 14 shows the SEM images of spot irradiation at a pulse fluence of 0.32 J/cm^2 and varying numbers of pulses.

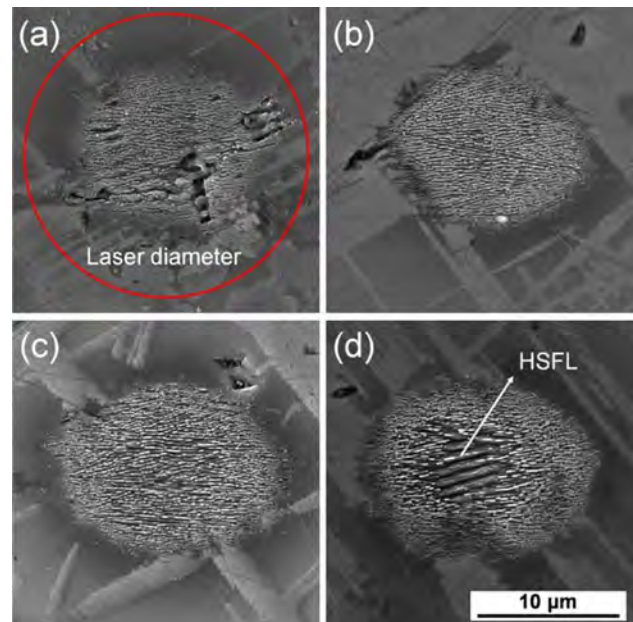


Fig. 14 SEM image of the spot irradiation carried with a fluence of 0.32 J/cm^2 at **a** 8, **b** 16, **c** 24, and **d** 32 pulses

For eight pulses, an HSFL formed on the entire area affected by the laser. The area affected by the laser is smaller than the laser spot size as the laser fluence on the edges was not high enough to cause any ablation. Moreover, the preexisting scratches expanded due to laser heating in Fig. 14a–c. Niitsu et al. reported a similar laser-induced crack expansion on single-crystal Si [41]. As the number of pulses was increased to 32, the LSFL started to form in the center while the HSFL remained on the edges. The formation of an LSFL, even at a low pulse fluence, is thought to be a result of the improved laser absorption

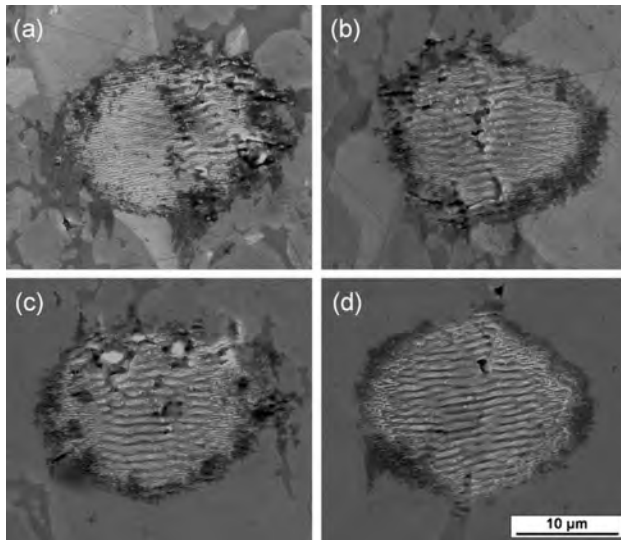


Fig. 15 SEM image of the spot irradiation carried with a fluence of 0.64 J/cm^2 at **a** 8, **b** 16, **c** 24, and **d** 32 pulses

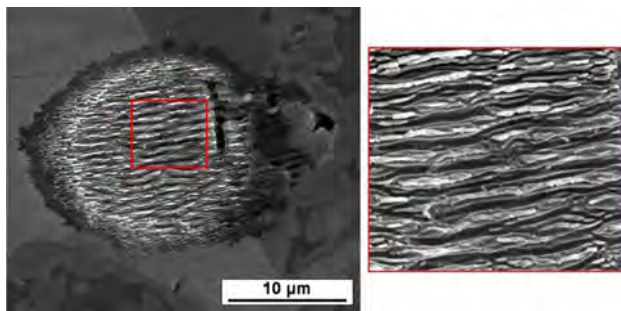


Fig. 16 SEM image of the spot irradiation experiment: first with 32 pulses at a fluence of 0.64 J/cm^2 and then with 16 pulses at a fluence of 0.32 J/cm^2

due to the elevated temperature and enhanced absorption by the HSFL due to the grating effect. Interestingly, the generated LSFL had a single HSFL LIPSS formation on the peak of the LSFL, whereas the HSFL did not form inside the valley of the LSFL. This finding suggests that after the LSFL formation, further irradiated pulses led to the formation of the HSFL on the LSFL.

Fluence was increased to 0.64 J/cm^2 , and the experiment was repeated. At eight pulses, an HSFL formed on the entire laser spot area, and the LSFL observed in Fig. 15b formed on the Si matrix, not on the SiC grain. At 16 pulses, the LSFL started to form on the SiC grain in the central area. For 24 pulses, the LSFL formed on most of the surface. Unlike the LSFL in Fig. 14d, due to the high pulse fluence, the LSFL formed, in this case, did not have an HSFL on the top of the LSFL. Finally, for 32 pulses, uniform LSFLs

formed on almost the entire spot area, except for the extreme edges of the spot. Interestingly, the hybrid LIPSS can be observed at the boundary between the HSFL and LSFL. The interaction between the HSFL and LSFL forming SPPs could have resulted in the formation of a hybrid LIPSS at the boundary.

Finally, spot irradiation was first carried out with 32 pulses at a fluence of 0.64 J/cm^2 and then with 16 pulses at a fluence of 0.32 J/cm^2 . A hybrid LIPSS can be observed in the central region in Fig. 16. This result supports the hypothesis that hybrid LIPSSs are a result of the laser fluence/intensity-dependent generation of two different SPPs on SiC.

5.3 Models for the LIPSS Formation

Figures 17 and 18 summarize the LIPSS formation mechanism of various LIPSSs. The reason for the LSFL formation on Si and SiC is due to the near-laser-wavelength SPP generation, which is generated during the free carrier generation-induced metallic state of Si/SiC under high laser intensities. As the bandgap of Si is near the photon energy of the laser, an HSFL was not observed on Si. Moreover, SiC has a bandgap around three times that of laser photon and thus does not readily absorb laser. Hence, at near-ablation-threshold laser pulse fluence, HSFLs form on SiC due to the third-harmonic generation, which is generated due to the third-order non-linear susceptibility ($\chi^{(3)}$) of SiC. Finally, a hybrid LIPSS formation is a combination of the HSFL and LSFL forming mechanisms. First, an HSFL is generated on the surface as SiC interacts with low laser intensity, as represented in zone 1 in Fig. 18. Then, the same region observes a much higher intensity leading to the LSFL formation, as shown in zone 2. Lastly, the intensity decreases to the HSFL formation range, which results in the third-harmonic generation at the bottom of the LSFL, which results in the HSFL formation at the bottom.

6 Conclusions

A fundamental investigation of the LIPSS formation on RB-SiC via femtosecond pulsed laser irradiation was carried out. The following conclusions were obtained:

- LSFL formation was observed on Si, and LSFL and HSFL formations were observed on SiC.
- The laser fluence threshold for the LIPSS formation on the edges of SiC grains and the entirety of small SiC grains was reduced due to the heat transfer by Si, which has enhanced laser absorption.

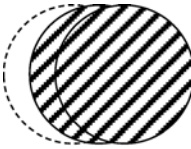
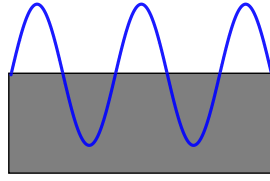
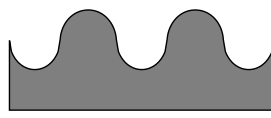
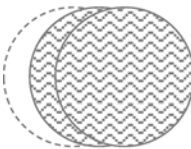
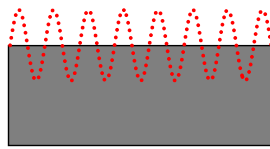
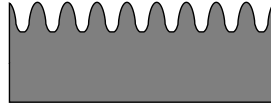
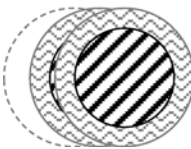
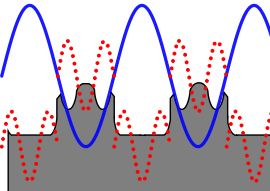
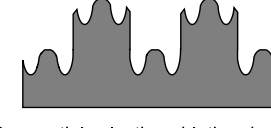
	Pulse fluence	SPP formation	LIPSS formation
(a)	<p>High pulse fluence</p>  <p>Intensity inside the spot is above LSFL forming threshold</p>	<p>$\lambda_{SPP_LSFL} \approx \lambda_{Laser}$</p>  <p>SPP with near laser wavelength is generated on the surface</p>	<p>LSFL formation</p>  <p>SPP interference with incoming laser results in selective ablation</p>
(b)	<p>Low pulse fluence</p>  <p>Peak intensity inside the laser spot is below LSFL forming threshold</p>	<p>$\lambda_{SPP_HSFL} \approx \lambda_{SPP_LSFL} / 3$</p>  <p>SPP with wavelength much smaller than laser wavelength is generated on the surface</p>	<p>HSFL formation</p>  <p>SPP interference with incoming laser results in selective ablation</p>
(c)	<p>Medium pulse fluence</p>  <p>The intensity in the central region is above the LSFL formation threshold, while edge is below the threshold</p>	<p>$\lambda_{SPP_Hybrid} : \lambda_{SPP_LSFL} \text{ \& } \lambda_{SPP_HSFL}$</p>  <p>LSFL and HSFL forming SPPs is generated on the surface sequentially</p>	<p>Hybrid LIPSS formation</p>  <p>Sequential selective ablation due SPP interference with laser results in hybrid LIPSS formation</p>

Fig. 17 LIPSS formation based on proposed SPP generation at a high pulse fluence b low pulse fluence and c medium pulse fluence

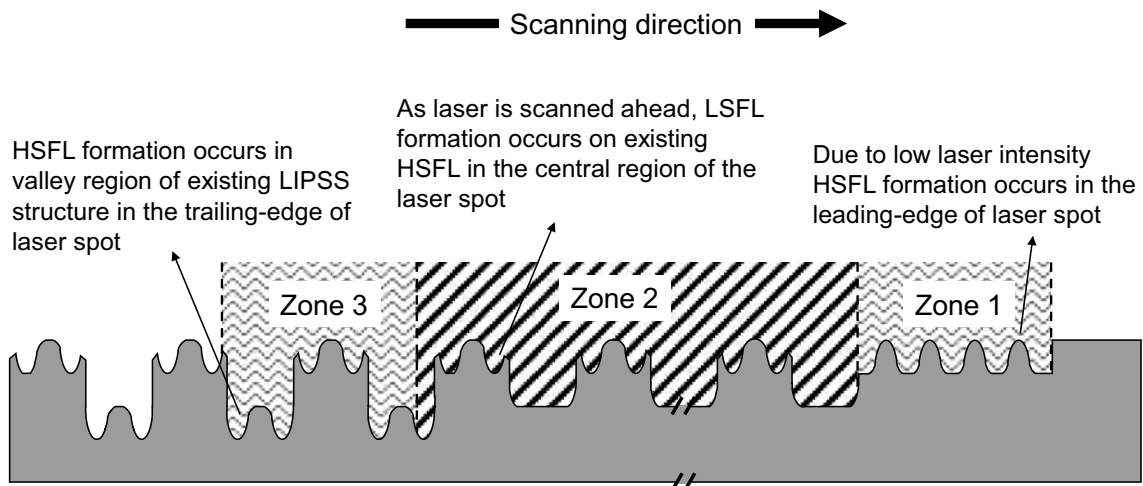


Fig. 18 Mechanism of the hybrid LIPSS formation based on the sequential formation of an HSFL and LSFL

- An HSFL–LSFL hybrid structure formed on SiC as a result of the interference of two different SEWs with the laser. The nonlinear response of SiC to the intensity of the laser is the main reason for the generation of these SEWs.
- Raman spectroscopy and TEM observation indicated that the hybrid LIPSSs were made of a single-crystalline SiC grain and did not show any amorphization.
- The effect of angle between laser polarization and scanning direction greatly affected the uniformity of the generated LIPSS. Clear uniform structures were generated when the laser was scanned parallel to the polarization direction.

The results of this study demonstrate the possibility of utilizing a laser to generate various complex surface structures on multiphase composite materials by taking advantage of differences and changes in the optical properties of the constituent material.

Author contributions Both authors read and approved the final manuscript.

Availability of data and materials The author declare that all data supporting the findings of this study are available within the article.

Declaration

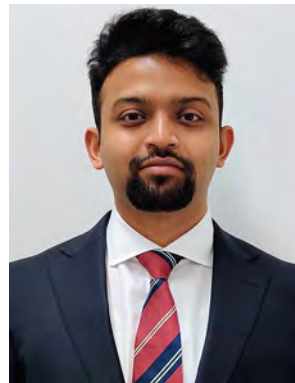
Conflict of interest Jiwang Yan is an editorial board member for “Nanomanufacturing and Metrology” and was not involved in the editorial review, or the decision to publish this article. All authors declare that there are no competing interests.

Open Access This article is licensed under a Creative Commons Attribution 4.0 International License, which permits use, sharing, adaptation, distribution and reproduction in any medium or format, as long as you give appropriate credit to the original author(s) and the source, provide a link to the Creative Commons licence, and indicate if changes were made. The images or other third party material in this article are included in the article's Creative Commons licence, unless indicated otherwise in a credit line to the material. If material is not included in the article's Creative Commons licence and your intended use is not permitted by statutory regulation or exceeds the permitted use, you will need to obtain permission directly from the copyright holder. To view a copy of this licence, visit <http://creativecommons.org/licenses/by/4.0/>.

References

1. Onaka T, Nakagawa T (2005) SPICA: a 3.5 m space infrared telescope for mid- and far-infrared astronomy. *Adv Space Res* 36:1123–1127. <https://doi.org/10.1016/j.asr.2005.05.087>
2. Suyama S, Itoh Y, Tsuno K, Ohno K (2005) NT-SiC (new-technology silicon carbide): Φ 650 mm optical space mirror substrate of high-strength reaction-sintered silicon carbide. p 58680E
3. Liew PJ, Yan J, Kuriyagawa T (2014) Fabrication of deep micro-holes in reaction-bonded SiC by ultrasonic cavitation assisted micro-EDM. *Int J Mach Tools Manuf* 76:13–20. <https://doi.org/10.1016/j.ijmactools.2013.09.010>
4. Yan J, Zhang Z, Kuriyagawa T (2009) Mechanism for material removal in diamond turning of reaction-bonded silicon carbide. *Int J Mach Tools Manuf* 49:366–374. <https://doi.org/10.1016/j.ijmactools.2008.12.007>
5. Zhang Z, Yan J, Kuriyagawa T (2011) Study on tool wear characteristics in diamond turning of reaction-bonded silicon carbide. *Int J Adv Manuf Technol* 57:117–125. <https://doi.org/10.1007/s00170-011-3289-3>
6. Vorobyev AY, Guo C (2008) Colorizing metals with femtosecond laser pulses. *Appl Phys Lett* 92:041914. <https://doi.org/10.1063/1.2834902>
7. Bonse J, Koter R, Hartelt M et al (2015) Tribological performance of femtosecond laser-induced periodic surface structures on titanium and a high toughness bearing steel. *Appl Surf Sci* 336:21–27. <https://doi.org/10.1016/j.apsusc.2014.08.111>
8. Buividas R, Stoddart PR, Juodkazis S (2012) Laser fabricated ripple substrates for surface-enhanced Raman scattering. *Ann Phys* 524:L5–L10. <https://doi.org/10.1002/andp.201200140>
9. Zorba V, Stratakis E, Barberoglou M et al (2008) Tailoring the wetting response of silicon surfaces via fs laser structuring. *Appl Phys A* 93:819–825. <https://doi.org/10.1007/s00339-008-4757-y>
10. Eichstät J, Römer GRBE, Huis in't Veld AJ (2011) Towards friction control using laser-induced periodic surface structures. *Phys Procedia* 12:7–15. <https://doi.org/10.1016/j.phpro.2011.03.099>
11. Bonse J, Rosenfeld A, Krüger J (2009) On the role of surface plasmon polaritons in the formation of laser-induced periodic surface structures upon irradiation of silicon by femtosecond-laser pulses. *J Appl Phys* 106:104910. <https://doi.org/10.1063/1.3261734>
12. Bonse J, Hohm S, Kirner SV et al (2017) Laser-induced periodic surface structures—a scientific evergreen. *IEEE J Sel Top Quantum Electron* 23:109–123. <https://doi.org/10.1109/jstqe.2016.2614183>
13. Miyaji G, Miyazaki K (2008) Origin of periodicity in nanostructuring on thin film surfaces ablated with femtosecond laser pulses. *Opt Express* 16:16265. <https://doi.org/10.1364/oe.16.016265>
14. Borowiec A, Haugen HK (2003) Subwavelength ripple formation on the surfaces of compound semiconductors irradiated with femtosecond laser pulses. *Appl Phys Lett* 82:4462–4464. <https://doi.org/10.1063/1.1586457>
15. Dufft D, Rosenfeld A, Das SK et al (2009) Femtosecond laser-induced periodic surface structures revisited: a comparative study on ZnO. *J Appl Phys* 105:034908. <https://doi.org/10.1063/1.3074106>
16. Kobayashi T, Wakabayashi T, Takushima Y, Yan J (2019) Formation behavior of laser-induced periodic surface structures on stainless tool steel in various media. *Precis Eng* 57:244–252. <https://doi.org/10.1016/j.precisioneng.2019.04.012>
17. Nakajima A, Omiya M, Yan J (2022) Generation of micro/nano hybrid surface structures on copper by femtosecond pulsed laser irradiation. *Nanomanuf Metrol*. <https://doi.org/10.1007/s41871-022-00135-9/figures/11>
18. Dar MH, Kuladeep R, Saikiran V, Rao ND (2016) Femtosecond laser nanostructuring of titanium metal towards fabrication of low-reflective surfaces over broad wavelength range. *Appl Surf Sci* 371:479–487. <https://doi.org/10.1016/j.apsusc.2016.03.008>
19. Chen F, Zhang D, Yang Q et al (2013) Bioinspired wetting surface via laser microfabrication. *ACS Appl Mater Interfaces* 5:6777–6792. <https://doi.org/10.1021/am401677z>
20. Polo JA, Lakhtakia A (2011) Surface electromagnetic waves: a review. *Laser Photonics Rev* 5:234–246. <https://doi.org/10.1002/lpor.200900050>
21. Gemini L, Hashida M, Shimizu M et al (2014) Periodic nanostructures self-formed on silicon and silicon carbide by femtosecond laser irradiation. *Appl Phys A Mater Sci Process* 117:49–54. <https://doi.org/10.1007/s00339-014-8502-4>

22. Huang M, Zhao F, Cheng Y et al (2009) Origin of laser-induced near-subwavelength ripples: interference between surface plasmons and incident laser. *ACS Nano* 3:4062–4070. <https://doi.org/10.1021/nn900654v>
23. Puerto D, Garcia-Lechuga M, Hernandez-Rueda J et al (2016) Femtosecond laser-controlled self-assembly of amorphous-crystalline nanogratings in silicon. *Nanotechnology* 27:265602. <https://doi.org/10.1088/0957-4484/27/26/265602>
24. Gemini L, Hashida M, Shimizu M et al (2013) Metal-like self-organization of periodic nanostructures on silicon and silicon carbide under femtosecond laser pulses. *J Appl Phys* 114:194903. <https://doi.org/10.1063/1.4832829>
25. Ganeev RA, Baba M, Ozaki T, Kuroda H (2010) Long- and short-period nanostructure formation on semiconductor surfaces at different ambient conditions. *J Opt Soc Am B* 27:1077. <https://doi.org/10.1364/josab.27.001077>
26. Rohlifing M, Krüger P, Pollmann J (1993) Quasiparticle band-structure calculations for C, Si, Ge, GaAs, and SiC using Gaussian-orbital basis sets. *Phys Rev B* 48:17791–17805. <https://doi.org/10.1103/physrevb.48.17791>
27. Karch K, Bechstedt F, Pavone P, Strauch D (1996) Pressure-dependent properties of SiC polytypes. *Phys Rev B Condens Matter Mater Phys* 53:13400–13413. <https://doi.org/10.1103/physrevb.53.13400>
28. Liu YH, Kuo KK, Cheng CW, Lee AC (2022) Femtosecond laser two-beam interference applied to 4H-SiC surface hierarchical micro-nano structure fabrication. *Opt Laser Technol* 151:108081. <https://doi.org/10.1016/j.optlastec.2022.108081>
29. Rohloff M, Das SK, Höhm S et al (2011) Formation of laser-induced periodic surface structures on fused silica upon multiple cross-polarized double-femtosecond-laser-pulse irradiation sequences. *J Appl Phys* 110:014910. <https://doi.org/10.1063/1.3605513>
30. Rosenfeld A, Rohloff M, Höhm S et al (2012) Formation of laser-induced periodic surface structures on fused silica upon multiple parallel polarized double-femtosecond-laser-pulse irradiation sequences. *Appl Surf Sci* 258:9233–9236. <https://doi.org/10.1016/j.apsusc.2011.09.076>
31. Obara G, Shimizu H, Enami T et al (2013) Growth of high spatial frequency periodic ripple structures on SiC crystal surfaces irradiated with successive femtosecond laser pulses. *Opt Express* 21:26323. <https://doi.org/10.1364/oe.21.026323>
32. Shi X, Xu X (2019) Laser fluence dependence of ripple formation on fused silica by femtosecond laser irradiation. *Appl Phys A Mater Sci Process* 125:1–8. <https://doi.org/10.1007/s00339-019-2554-4>
33. Casquero N, Fuentes-Edfuf Y, Zazo R et al (2020) Generation, control and erasure of dual LIPSS in germanium with fs and ns laser pulses. *J Phys D Appl Phys* 53:485106. <https://doi.org/10.1088/1361-6463/abafdf>
34. Gerasimov VV, Knyazev BA, Kotelnikov IA et al (2013) Surface plasmon polaritons launched using a terahertz free-electron laser: propagation along a gold–ZnS–air interface and decoupling to free waves at the surface edge. *J Opt Soc Am B* 30:2182. <https://doi.org/10.1364/josab.30.002182>
35. Liu W, Jiang L, Han W et al (2019) Manipulation of LIPSS orientation on silicon surfaces using orthogonally polarized femtosecond laser double-pulse trains. *Opt Express* 27:9782. <https://doi.org/10.1364/oe.27.009782>
36. Zazo R, Solis J, Sanchez-Gil JA et al (2020) Deep UV laser induced periodic surface structures on silicon formed by self-organization of nanoparticles. *Appl Surf Sci* 520:146307. <https://doi.org/10.1016/j.apsusc.2020.146307>
37. Guo X, Peng Z, Ding P et al (2021) Nonlinear optical properties of 6H-SiC and 4H-SiC in an extensive spectral range. *Opt Mater Express* 11:1080. <https://doi.org/10.1364/ome.415915>
38. De Leonardis F, Soref RA, Passaro VMN (2017) Dispersion of nonresonant third-order nonlinearities in silicon carbide. *Sci Rep* 7:1–12. <https://doi.org/10.1038/srep40924>
39. Guo Y, Deutsch M (2010) Third harmonic generation using surface plasmon polaritons at nonlinear interfaces. In: *Optics InfoBase conference papers*, pp 3–4. <https://doi.org/10.1364/fio.2010.fwn5>
40. De Hoogh A, Opheij A, Wulf M et al (2016) Harmonics generation by surface plasmon polaritons on single nanowires. *ACS Photonics* 3:1446–1452. <https://doi.org/10.1021/acsp Photonics.5b00686>
41. Niitsu K, Yan J (2020) Effects of deep subsurface damages on surface nanostructure formation in laser recovery of grinded single-crystal silicon wafers. *Precis Eng* 62:213–222. <https://doi.org/10.1016/j.precisioneng.2019.12.005>



Tushar Meshram received his Bachelor's degree in Mechanical Engineering from Indian Institute of Technology, Hyderabad in 2017. He is currently a Ph.D. student at Keio University, Japan, under the supervision of Prof. Yan. His research interests include laser processing and micro/nano manufacturing on high bandgap semiconductor material.



Jiawang Yan received his Ph.D. from Tohoku University, Japan in 2000 and is currently a professor of Mechanical Engineering at Keio University (2012–now), leading the Laboratory for Precision Machining and Nano Processing. His research areas include ultraprecision machining, micro/nano manufacturing, laser processing, nanomaterials, and nanomechanics.